The brittle and ductile components of displacement along fault zones

Catherine Homberg, Johann Schnyder, Virginie Roche, Véronique Léonardi, Mohamed Benzaggagh

The brittle and ductile components of displacement along fault zones

C. HOMBERG[1,2]*, J. SCHNYDER[1,2], V. ROCHE[3], V. LEONARDI[4] & M. BENZAGGAGH[5]

[1]*Sorbonne Universités, UPMC Université Paris 06, UMR 7193, Institut des Sciences de la Terre de Paris (ISTeP), F-75005, Paris, France*

[2]*CNRS, UMR 7193, Institut des Sciences de la Terre de Paris (ISTeP), F-75005, Paris, France*

[3]*Fault Analysis Group, School of Earth Sciences, University College of Dublin, Dublin, Ireland*

[4]*HSM Montpellier, UMR 5569, Université de Montpellier, CC57, 34090 Montpellier, France*

[5]*University Moulay Ismail, Faculty of Sciences, BP 11.201, Jbabra, Zitoune, Meknès, Morocco*

**Correspondence: catherine.homberg@upmc.fr*

Abstract: The total offset across a fault zone may include offsets by discontinuous faulting as well as continuous deformation, including fault-related folding. This study investigates the relationships between these two components during fault growth. We established conceptual models for the distributions of displacement due to faulting (i.e. brittle component or near-field displacement), to folding (i.e. ductile component) and to the sum of both (i.e. far-field displacement) for different mechanisms of fault-related folding. We then compared these theoretical displacement profiles with those measured along mesoscale normal faults cutting carbonate-rich sequences in the Southeast Mesozoic sedimentary basin of France. The near-field and far-field displacement profiles follow either a flat-topped or a triangular shape. Several fold mechanisms were recognized, sometimes occurring together along the same fault and represent either fault-propagation folds, shear folds or coherent drag folds. In the last case, local deficit in the fault slip is balanced by folding so that the brittle and ductile components compose together a coherent fault zone. Common characteristics of these faults are a high folding component that can reach up to 75% of the total fault throw, a high displacement gradient (up to 0.5) and a strong fault sinuosity.

Faults in the upper crust form complex zones of deformation where discontinuous offsets along slip surfaces dominate (i.e. brittle deformation). Various amounts of continuous deformation like folding (i.e. ductile deformation) also occur around fault planes (e.g. Ferrill & Morris 2008; Ghalayini *et al.* 2016). These fault-related folds have a major role in several geological issues. First, they are key elements for petroleum systems as they may form structural traps and affect reservoir communication across the faults (e.g. Ferrill *et al.* 2005). Second, they account for part of the co-seismic deformation of the Earth surface and provide useful information to assess earthquake hazards (e.g. Allmendinger & Shaw 2000). Third, the stratigraphic response to synsedimentary faulting is strongly influenced by the folding component (e.g. Gawthorpe *et al.* 1997).

Fault-related folds are observed in all tectonic settings and have been classified according to their mechanical origin or to the geometrical configuration in which they occur (e.g. Schlische 1995; Janecke *et al.* 1998; Ferrill *et al.* 2005; Brandes & Tanner 2014). A short review of the most common ones in extensional and compressional settings is given below. Fault-bend folds (Fig. 1a) are associated with non-planar fault geometries. They have been extensively documented in thrust systems with flat and ramp geometries (e.g. Suppe 1983; McClay 1992; Calamita *et al.* 2012) where layers are passively folded when they pass above a thrust ramp. Similar dip variations are also commonly observed along mesoscale normal faults cutting layered media (Mandl 1988; Ferrill & Morris 2003; Schöpfer *et al.* 2007; Roche *et al.* 2012*a*). A listric normal fault (Fig. 1b) is a special type of non-planar fault geometry where layers in the hanging wall are folded in a rollover structure. In this case, the layers are concave in the direction of slip (i.e. reverse 'drag').

Folds between fault segments are associated with segmented fault zones (Fig. 1c). In neutral relays, the relay ramp forms a well-expressed tilted surface between the two segments (e.g. Peacock & Parfitt 2002). Folding also occurs in relay zones observed in cross-sections (e.g. Nicol *et al.* 2002; Koledoye *et al.* 2003; Rotevatn & Jackson 2014).

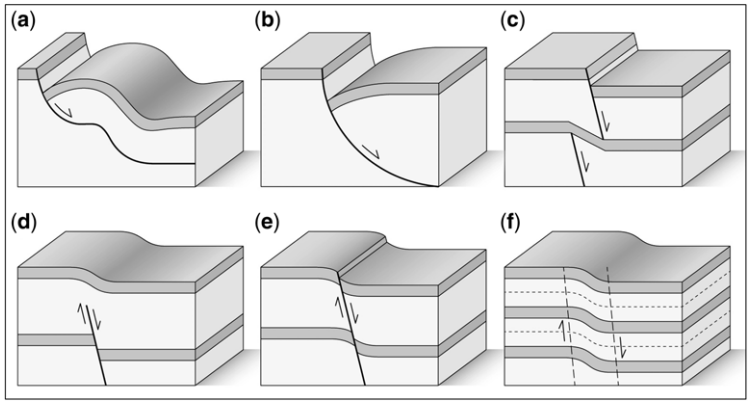

Fig. 1. Diagrams of the common types of fault-related folds: (**a**) fault-bend fold; (**b**) rollover anticline along listric fault; (**c**) fold between fault segments; (**d**) fault-propagation fold; (**e**) drag fold; and (**f**) shear fold. The folding mechanisms in (a) and (c)–(f) are drawn for normal faulting but are also common along reverse faults.

In both cases, the relays may later breach the folded layers.

Fault-propagation folds (Fig. 1d) are generally observed in rocks with contrasted mechanical properties such as sediment infillings lying above a crystalline basement (i.e. forced folds), or clay-rich units alternating with stiff limestones or sandstones (e.g. Withjack *et al.* 1990; Ferrill *et al.* 2007). Usually, the soft sediments are folded ahead of the fault tip due to movement of the hanging wall along a fault imbedded in the rigid unit. Once the folded rock at the fault tip fails, the fault propagates forwards, offsetting the folded layers. Such folding may be localized ahead of a fault that is no longer able to propagate in the vertical direction (Roche *et al.* 2012*b*). Alternatively, the folding may reflect ductile deformation occurring in the course of the vertical propagation of the fault, among other processes occurring at the fault tip.

In their original description, drag folds (Fig. 1e) occur in the fault wall rocks as a consequence of the frictional resistance to slip (e.g. Cloos 1936), but this interpretation has been challenged: Grasemann *et al.* (2005) proposed that drag folds are caused by the heterogeneous displacement field around a fault as it undergoes slip. Ferrill *et al.* (2012) proposed that an apparent 'drag' structure is not the product of frictional sliding: instead, it is originally formed at the fault tip before being offset by the fault. Finally, shear folds (Fig. 1f) develop in shear zones and represent the most ductile expression of fault zones. Shear folds are expected to occur at mid to deep levels of the crust (e.g. Carreras *et al.* 2005), but may also develop during gravitational instabilities or other deformation processes affecting unlithified sediments.

All these types of folds have been recognized at various scales and may present distinct characteristics (see Janecke *et al.* 1998; Schlische 1995; Ferrill *et al.* 2005; Brandes & Tanner 2014 for a review). However, it may be difficult to interpret natural cases of fault-related folds because several types of folding can be localized in the same area. They can form simultaneously due to the superposition of several processes or they can form at different times in the fault history and then become superposed during fault growth.

A routine method to assess fault-related folds is to use kinematic approaches, like the kink fold or trishear models (Suppe 1983; Suppe & Medwedeff 1990; Erslev 1991; Zoetemeijer *et al.* 1992; Allmendinger 1998). Numerical approaches strengthened the need to include a mechanical foundation as deformation is strongly influenced by the mechanical stratigraphy (e.g. Finch *et al.* 2004; Smart *et al.* 2012). However, despite the abundant literature on fault-related folds, quantitative data on the folding component along fault zones are still sparse (Mansfield & Cartwright 1999; Long & Imber 2010; Ferrill *et al.* 2011, 2012), and it is challenging to make a proper distinction between the different folding processes on geometrical criteria.

This study aims to investigate the relationship between the folding and fault-slip components during fault growth. First, we propose theoretical models showing the distribution of the discontinuous offsets (i.e. brittle component or near-field displacement), the folding (or ductile) component of the displacement and the sum of both (i.e. far-field displacement). For each case, we evaluate the degree of overlap or diagnostic values for the different tested fold mechanisms. Then, based on these different models, we examine mesoscale normal faults cutting through carbonate-rich sequences in the Southeast Mesozoic sedimentary basin of France. We do not intend to give an exhaustive

description of fold mechanisms or to document them by statistical means. Instead, we aim to evaluate the possible combinations of ductile and brittle deformation, using a methodology that integrates the ductile component in the fault analysis. Finally, we discuss how far-field and near-field displacement–length plots reveal important aspects of fault growth, and emphasize the role of the rheological properties of the faulted lithologies.

Conceptual models of near-field and far-field displacements along blind normal faults

Brittle and ductile components of the fault movement

Conceptual models comparing the brittle component (i.e. through a displacement discontinuity) and the ductile component (i.e. through continuous displacement) of the fault movement are presented below. Three mechanisms of fault-related folding are investigated: fault-propagation folds (Fig. 1d); simple shear folds (Fig. 1f); and a special kind of drag fold (Fig. 1e) referred to as coherent drag folds. These three kinds of folds have their axis sub-parallel to the fault strike and accommodate a continuous offset in sympathy with the fault slip (referred to as normal folding, positive drag, synthetic beds or displacements by various authors: e.g. Mansfield & Cartwright 1999; Ferrill *et al.* 2005; Brandes & Tanner 2014). They affect a variable width of the fault walls depending on their wavelength. Their contributions to the total displacement depend on their amplitude.

The methodology we proposed in this article allows comparison between the predictions of those models with measurements on natural faults observed in cross-section. Such measurements can be acquired in the field, from 3D seismic data or from analogue sand-box experiments. Even though we focus here on blind normal faults, our approach can also be applied to reverse faults. We define the near-field displacement as the offset measured at the fault plane (Fig. 2). The far-field displacement is measured at a distance from the fault plane. For the faults considered here, the near-field displacement corresponds to the strain produced by faulting, and the far-field displacement includes both faulting and folding. The folding component of the throw is therefore obtained by subtracting the near-field displacement from the far-field displacement. Similar methodologies have been used for faults observed along their strike in seismic data by Long & Imber (2010).

In all cases considered here, we assume the slip profiles during fault growth are as shown in Figure 2. In the early fault history, the near-field displacement distribution follows a triangular shape (i.e. with constant gradient). During later slip episodes, the displacement is constant along the pre-existing fault portion and decreases linearly to zero with the same displacement gradient along the newly formed fault portion. This model results in a triangular displacement profile at any time during the fault history that fits with the observations on isolated faults growing in a homogenous rock (Muraoka & Kamata 1983; Walsh & Watterson 1987; Soliva *et al.* 2005; Roche *et al.* 2012*b*). Because measuring the bed offset down the fault dip may involve large uncertainties when the fault trace is irregular, we prefer to use the fault throw: that is, the bed offset measured in the vertical. We refer to it below as the fault displacement to follow the nomenclature used in displacement profiles analysis.

Fault-propagation folds

The different displacement profiles along a normal fault in front of which a fault-propagation fold develops are shown in Figure 2a. Along the fault plane, the near-field displacement decreases from a maximum to zero at the fault tips. No folding component occurs along the fault plane so that the far-field displacement equals the near-field displacement. Ahead of the fault tip, the fold (or monocline) accommodates a vertical displacement along a distance referred to as the damping distance. The folding component increases abruptly and remains constant along most of the damping distance before finally falling to zero. The vertical dimension of this distance is likely to be sensitive to rock lithology. This will be discussed further in the 'Discussion' section, later in this paper. Eventually, the fault propagates forwards and cuts the fault-tip fold, which does not then accumulate further strain. This situation is expressed by diverging near-field and far-field curves, the point of divergence marking the initial fault tip (Fig. 2a).

Simple shear folds

A ductile shear zone represents the extreme case of very compliant rocks in which the strain is accommodated entirely through folding. The near-field displacement is thus zero all along the shear zone (Fig. 2b). With increasing strain, subsequent development of a brittle fault cutting the folded zone modifies the displacement profiles. If the displacement was constant along the shear zone, the mathematical translation that links the near-field and far-field data of the final fault zone is easily recognized on the displacement plots. Both near-field and far-field profiles will then show a triangular

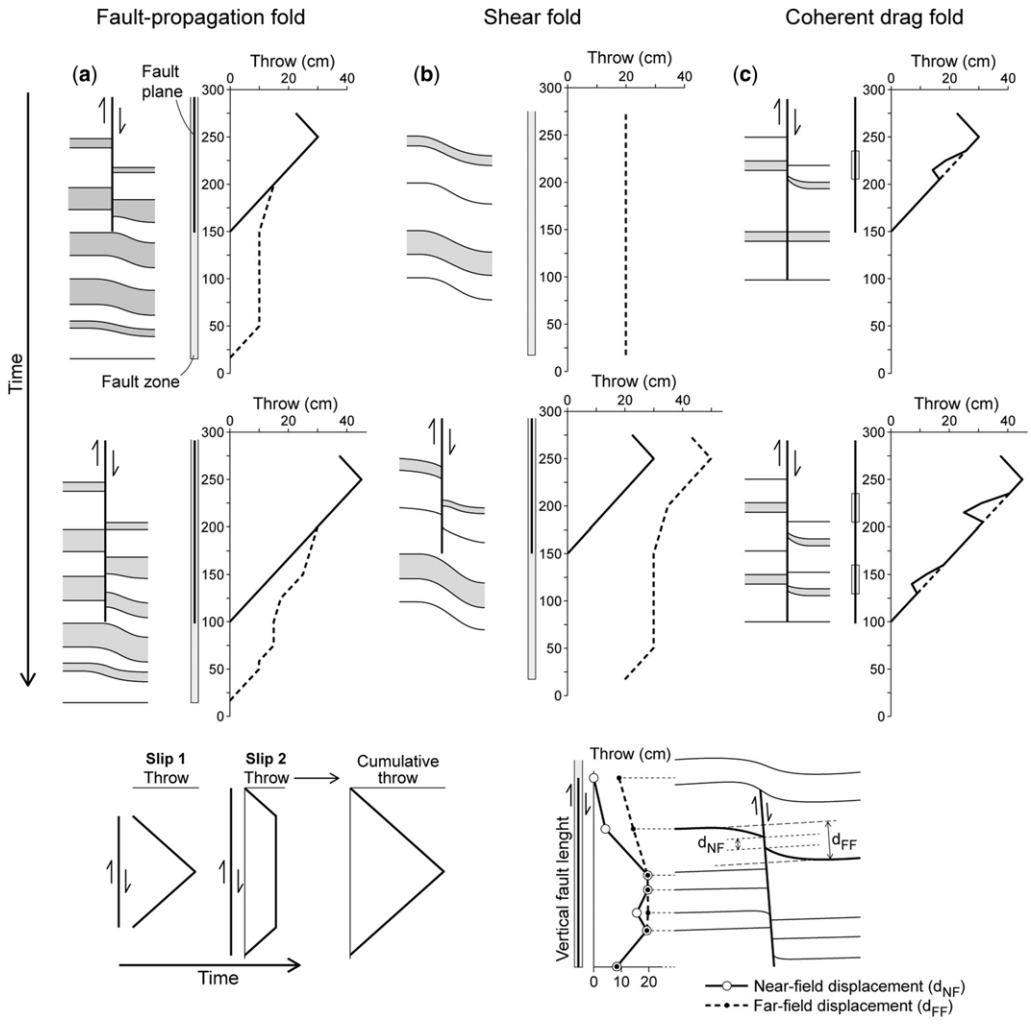

Fig. 2. Conceptual models of displacement distribution for different mechanisms of fault-related folding: (**a**) fault-propagation folds; (**b**) shear folds; and (**c**) coherent drag folds. Inset shows the slip model during fault growth and the procedure for displacement data acquisition. The near-field displacement (d_{NF}) is measured at the fault plane and corresponds to the throw achieved by fault slip. The far-field displacement (d_{FF}) is measured at a distance from the fault plane and accounts for the total offset, and includes both the faulting and folding components. Displacement profiles are constructed by plotting the displacement data along the fault height.

shape. Ahead of the fault plane, the far-field displacement is constant and its value equals the magnitude of the translation vector. If the displacement profile along the shear zone was triangular, the folding component will vary along the fault zone and the far-field displacement profile will become more irregular. The relationship between the final far-field and near-field displacement profiles allow us to distinguish between shear folds later cut by a fault and fault-propagation folds (cf. Fig. 2a, b). In particular, faults in which shear folds developed always show far-field displacement values that are greater than the near-field ones, even at the point of maximal far-field displacement.

Coherent drag folds

The last case considers a fault zone along which folding and faulting occur, and combines them together at specific levels. In this case, although the brittle and ductile components of the total offset may fluctuate along the fault zone (Fig. 2c), these fluctuations are complementary and when summed yield a ‘coherent fault zone’. Following the

descriptive term of drag fault, we refer to this type of fault-related fold as a 'coherent drag fold'. Faults with coherent drag folds show quite different far-field and near-field profiles. The far-field profile shows a regular triangular shape, whereas the near-field displacement and the folding component exhibit small-scale fluctuations (Fig. 2c). Notably, in the coherent drag-fold model, these fluctuations balance each other so that the total strain (achieved by both folding and faulting) shows a regular far-field profile.

These conceptual models represent ideal cases isolating the effect of each fold type. The three cases considered here show different combinations of near-field and far-field profiles, and the shapes of these profiles can be useful in identifying the mechanism causing the development of fault-related folds, although the geological setting and fault history may be more complex for natural cases than the one described here. In the next section, we will compare the model predictions with data collected on mesoscale faults observed in the field.

Mesoscale normal faults in the Southeast Basin of France

Studied faults and regional context

We studied 12 normal faults in the Southeast sedimentary basin of France (Fig. 3). They have a maximum offset ranging from a few centimetres to a few tens of centimetres, with a variable amount of fault-related folding (Figs 4 & 5). They were observed in cross-sections in five outcrops nearby Sahune and Villeperdrix villages, in the Aulan Gorge, and in a natural excavation in the Agnielles Gorge, respectively (Fig. 3). Five faults cut deposits of Tithonian age in Villeperdrix (i.e. three faults named Fv1, Fv2 and Fv3) and in Agnielles (i.e. two faults named Fag1 and Fag2). Seven other faults

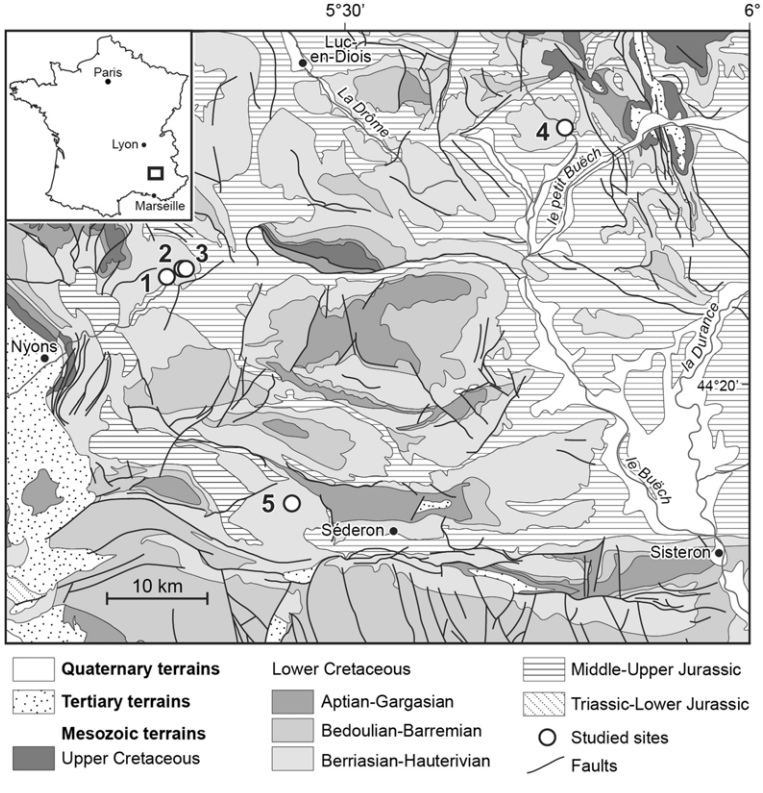

Fig. 3. Simplified geological map and studied sites. Circles with numbers are sites of observation: (1) Sahune (five faults: Fs1, Fs2, Fs3, Fs5 and Fs6); (2) Villeperdrix1 (one fault: Fv1); (3) Villeperdrix2 (two faults: Fv2 and Fv3); (4) Agnielles (two faults: Fag1 and Fag2); and (5) Aulan (two faults: Fau1 and Fau2). Geological contours and faults are from the 1/250 000 geological map of Valence (Rouire *et al.* 1980). The square shows the geographical location of the study area in France.

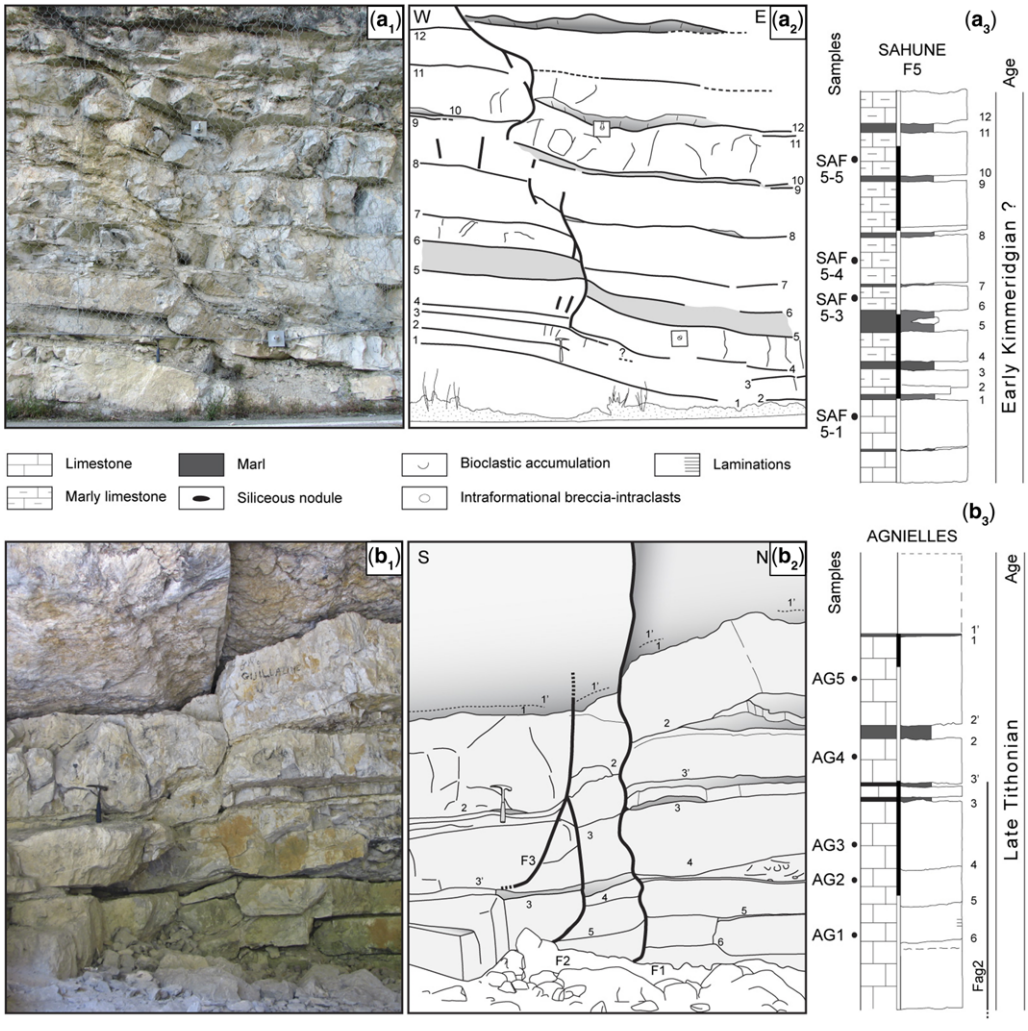

Fig. 4. Faults and hosting rocks. (**a**) & (**b**) Examples of faults Fs5 (at Sahune) and Fag1 (at Agnielles), and the lithology of the rocks. Both uninterpreted (a_1 and b_1) and interpreted photographs (a_2 and b_2) are shown, as well as the stratigraphic logs of the host rocks (a_3 and b_3). Samples used for thin section are shown. Bed surfaces used for displacement measurement are indicated with numbers. The correlation of markers in the central part of Agnielles section is not obvious. The same bed succession is, however, clearly recognized on the southern and northern continuation of the outcrop. There is thus no ambiguity about the cumulative fault offset. The position of Fag2 is indicated with a thick line on the right-hand side of stratigraphic log. The hammer indicates the scale. The scale in stratigraphic logs is indicated with alternating back and white thick lines, each one representing 1 m. See Figure 3 for the site location.

cut the Kimmeridgian and Valanginian sequences in Sahune (i.e. five faults named Fs1, Fs2, Fs3, Fs5 and Fs6) and Aulan (i.e. two faults named Fau1 and Fau2). These stratigraphic intervals are carbonate-rich, pelagic sequences and are described in the next subsection.

The outcrops are located in the Vocontian Trough, an east–west-trending sub-basin in the approximately 40 000 km^2 Southeast Basin of France. The latter developed during Mesozoic time due to the opening of the western Tethys (or ligurian Tethys). Up to 10 km of sediment infill accumulated in the basin (Dubois & Delfaud 1989). The overall basin history is well established: extension lasted from the Early Triassic to the Mid-Cretaceous, with a main rifting phase in Early–Mid Jurassic time, followed by several moderate intensity extensional periods (e.g. Debrand-Passard

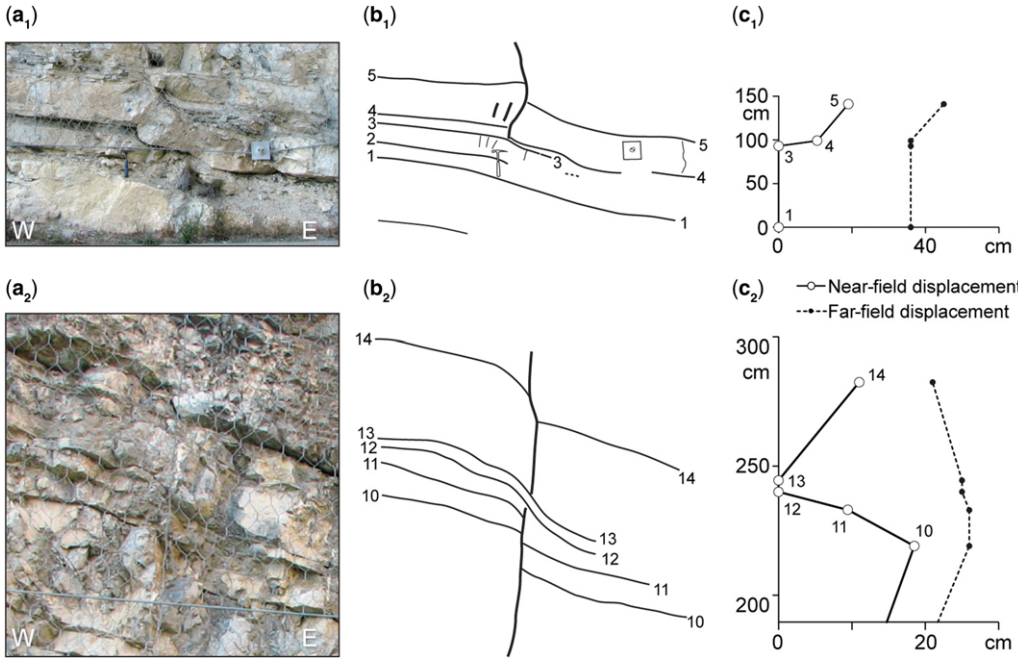

Fig. 5. Examples of fault-related folds. (**a$_1$**) & (**a$_2$**) Outcrop photograph of a detailed part of Fs5 and Fs2. (**b$_1$**) & (**b$_2$**) and (**c$_1$**) & (**c$_2$**) Interpreted photographs and displacement data. Analysis of displacement data along the full length of these faults suggests a composite origin for the folding component. The folds are interpreted as shear folds amplified by fault-propagation folding along Fs5 and coherent drag folding along Fs2. See the section on 'Fault geometry and displacement profiles' and Figure 8 for details.

et al. 1984; Dubois & Delfaud 1989; Homberg *et al.* 2013). During this long-lived extension, faults of various sizes developed, with a main NE–SW trend, and additional east–west and north–south trends (Lemoine *et al.* 2000 and references herein). The north–south faults observed in the Kimmeridgian and Tithonian sequences of Sahune and Villerperdrix are in line with the discrete Late Jurassic event during which synsedimentary faults developed in the Southeast Basin of France (Dardeau *et al.* 1988; Homberg *et al.* 2013). The east–west faults observed in the Late Tithonian and Valanginian sequences at Agnielles and Aulan are thought to be related to the major tectonic reorganization in Early Cretaceous time as a consequence of the opening of the Atlantic Ocean (Graciansky & Lemoine 1988; Homberg *et al.* 2013). At that time, a northwards slope–basin transition developed in the Ventoux–Lure area and sediments were redistributed via deep marine valleys with an approximately east–west trend (e.g. Joseph *et al.* 1989; Friès & Parize 2003; Homberg *et al.* 2013). Later deformation is associated with several periods of inversion, except during the Eo-Oligocene rifting, during which NNE–SSW normal faults developed in Western Europe (Bergerat 1987).

Rock lithology

A bed-by-bed survey has been performed in the field on the Villeperdrix, Agnielles and Sahune outcrops. This was complemented by a petrographical analysis of 31 thin sections (Figs 4 & 6) in order to characterize the main rock features and the sedimentary facies in the microscope. In each outcrop, the section under consideration encompassed all beds cut by the normal faults, and those lying above and below the upper and lower fault tips when visible. Rock dating was based on the microfauna associations because ammonites are rare in the studied sections.

Sahune sections. Fs1, Fs2, Fs3 and Fs6 cut through the same 4.8 m-thick sedimentary pile named here the Sahune Fs1-2 section. The lithology consists mainly of fine-grained limestone beds that are 5–53 cm thick and alternated sometimes with thin lenses of marl usually less than 5 cm thick (Fig. 6a). The limestone beds are composed of micrites (mudstones to wackestones and rare packstones) with rare bioclasts, including radiolarians, *Globochaete*, probable filaments, fragments of crinoids (*Saccocoma*), rare foraminifers and pelecypods.

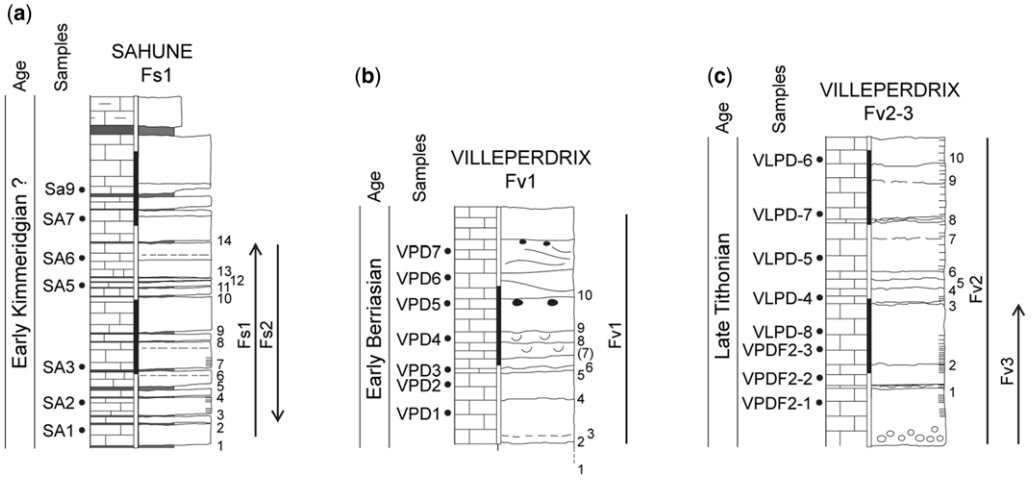

Fig. 6. Stratigraphic logs of the faulted medium. (**a**)–(**c**) The Sahune Fs1-2, Villeperdrix Fv1 and Villeperdrix Fv2-3 sections. Estimated sequence ages are on the left. They are inferred from calcisphaera species, except at the Sahune section. Thin lines indicate the position of the faults within the sequences, with arrows if tips are observed. Bed surfaces used for displacement measurement are indicated with numbers. The scale on the stratigraphic logs is indicated with alternating black and white thick lines, each one representing 1 m. See the legend in Figure 4.

The Sahune Fs5 section is 4.65 m thick and comprises limestone to marly limestone beds (20–59 cm thick) alternating with marly intervals (3–28 cm) (Fig. 4a). The microfacies are almost homogeneous in these beds and consist of micrite (mudstone) with rare bioclasts (radiolarians). This section thus includes several marly intervals, which is different from the Fs1-2 section described previously that consists mostly of limestone beds. In both sections, the limestone beds are generally homogeneous. The absence of *Saccocoma*, together with the rare microfauna, suggest a possible Early Kimmeridgian age, in agreement with the 1:50 000 geological map (Flandrin 1975).

Agnielles section. The Agnielles section is 3.3 m thick and consists of thick well-bedded fine-grained limestones (9–75 cm thick) alternating with thin marly intervals (generally <5 cm and up to 11 cm) (Fig. 4b). The microfacies correspond to *Saccocoma*–rich mudstones to wackestones, together with *Globochaete*. Samples yielded *Chitinoidella boneti* (Doben), which marks the base of the Late Tithonian (equivalent to the *Microcanthum* Ammonite Zone: Benzaggagh & Atrops 1995*a*). Similar to the Sahune sections, the micro-facies in the Agnielles section are rather homogeneous within each limestone bed, as well as from bed to bed.

Villeperdrix sections. The Villeperdrix Fv1 section is 3 m thick and consists of fine-grained limestone beds (5–58 cm thick) (Fig. 6b). This section yielded a high bioclastic content in specific levels, and brecciated layers and nodular chert levels. Limestone beds correspond to mudstones to wackestones often rich in radiolarians, *Globochaete* and calcisphaera. Numerous *Calpionella alpina*, rare *Crassicollaria parvula*, *Tintinnopsella carpathica* and *Remaniella ferasini* give an Early Berriasian age (B2 subzone of calpionellids: Benzaggagh & Atrops 1995*b*). Samples VPD5 yielded reworked intraclasts rich in *Crassicollaria parvula* and small *Calpionella alpina*, indicating a slightly older Early Berriasian age (B1 subzone of calpionellids).

The Villeperdrix Fv2-3 section is 4.18 m thick (Fig. 6c), and contains the Fv2 and Fv3 faults. The lithology consists of coarse-grained, finely laminated limestones passing into fine-grained, often laminated limestones (4–83 cm in thickness). Coarse-grained intervals correspond to micro-conglomeratic beds with infra-millimetric to centimetric mudstone lithoclasts and peloids (packstones) with calcisphaera, which occasionally yield echinoderm-rich laminations. Fine-grained intervals are wackestones with *Globochaete*, radiolarians, calcisphaera and, locally, *Saccocoma* or Aptychi. The genus *Crassicollaria* largely dominates among the *Calpionella alpina*, indicating a Late Tithonian age (A3 subzone of calpionellids: Remane 1971). In the bottom part of the section, sample VPDF2-1 yielded *Saccocoma*, which suggests a Late Tithonian (A2 subzone of calpionellids) age. Sections in Villerperdix thus differ from those in other sites in their grain size which is variable throughout the section and also within each limestone bed.

Aulan section. The Fau1 and Fau2 sections in Aulan consist of fine-grained limestone beds (20–30 cm in thickness) separated by very thin marly intervals (<5 cm thick). These sections were not sampled for micro-facies and fossil identification. According to the outcrop inspection, the limestones are composed of micrites (mudstones–wackestones). The Aulan section resembles the Fs1-2 section in Sahune and that in Agnielles.

Fault data acquisition

The 12 faults studied are generally composed of several closely spaced fractures, usually one or more slip surfaces, as well as thin calcite veins. We examined all fractures from the lower to the upper part of every fault and transcribed them onto scaled photographs (Fig. 4). The fault features were obtained precisely along each fault. When the upper parts of the faults were not accessible with a ladder (such as for Fs1 and Fs2), displacements were measured on pictures scaled with a ruler that was aligned along the normal of the bedding plane using a compass and a clinometer.

For each fault, we measured the strike and dip of the main slip surfaces. The slip vector was measured when visible (which was rare) and the criteria indicating the sense of motion were examined carefully. We located precisely each orientation result within the sedimentary sequence in order to recognize possible changes caused by the mechanical layering such as fault refractions: that is, a change in the fault dip through a bed interface ('bed-to-bed' data). Within a homogeneous bed, the surface of the fault often displays a sinuous shape (i.e. a progressive variation in the dip). In some extreme instances, dip variations are so important that the fault locally changes from normal to apparently reverse offset. In order to characterize the sinuosity inside a bed, we measured the maximum and minimum fault dip and strike values within a bed ('in-bed' data). The uncertainties for the strike and dip measurements were less than 2° for all faults, except for strike data on the faults in Sahune. In this locality, a wire mesh covering the outcrop created a magnetic disturbance resulting in an approximate strike value of the fractures. In all but the Sahune sites, the inclinations of the layering ranged from 5° to 10°. Thus, bed tilting did not significantly modify the fault orientation. In the Eygues Valley, the beds dip up to 20° at the Sahune site. Palaeostress determinations and analysis of conjugate mesoscale faults indicate that the north–south faults in this valley formed prior to tilting (Homberg *et al.* 2013). We have therefore restored the original orientations of the fractures in Sahune using ROTILT (Angelier 1990).

The top and bottom of the limestone beds, as well as a few internal interfaces within the limestones, were used as markers to establish how the displacement varies along each fault (Figs 4 & 5). Because the fault traces showed frequent irregularities in cross-section, we have measured the throw instead of the displacement along the fault plane. The bed offsets were measured very close to and at a distance (generally several decimetres and up to several metres) from the fault plane in order to distinguish the brittle (through a displacement discontinuity) and the ductile (through folding) component of the throw. Displacement data were then plotted against the vertical distance to construct profiles of the near-field and far-field displacements and the folding component, as shown at the beginning of this paper (Fig. 8). This measurement procedure was followed in order to examine how the deformation varies along a fault zone whatever the geometry of the slip surface and for various combinations of brittle and ductile deformation. When the fault included overlapping segments (Fag1), the cumulative displacement profile was also calculated by summing the displacements on each individual fault segment. Uncertainties on displacements and bed-to-bed distances are less than 0.5 cm and slightly higher, but probably less than 2 cm, along the upper parts of Fs1 and Fs2.

Fault geometry and displacement profiles

Fault shape and fault kinematics

The investigated normal faults are partly or completely exposed along vertical cross-sections (Fig. 4; Table 1) and observed along a vertical length ranging from 1 to 3 m (length of observation <30 cm for Fs3). A continuous bed interface marks the lower tip of Fs3, Fs5 and Fau1, and the upper tip of Fau2, Fs1, Fv3 and Fag2. Both tips of Fs2 and Fau2 were observed (with another segment existing ahead Fs2), whereas Fag1, Fs6, Fv1 and Fv2 cut through the whole outcropping section. Faults observed along their entire lengths allow a full description of the relationship between folding and faulting along the fault zone. Those incompletely exposed are also integrated in this study because they provide important quantitative information on the folding component and other key features.

Rare striations observed on these faults (Fag1, Fs1 and Fv2) are subhorizontal and are indicative of strike-slip movement. These striations are attributed due to minor fault reactivation during Late Cretaceous–Cenozoic inversion and are unrelated to the displacements recorded here which developed under a normal faulting regime. There is abundant evidence for Late Jurassic normal faulting in the Southeast Basin of France in the form of stratigraphic thickness changes across north–south faults,

Table 1. *Geometric fault attributes*

	Global attributes							'In-bed' variations		'Bed-to-bed' variations	
	L[1]	D_{max}[2]	Ti_l[3]	Ti_u[4]	F[5]	Strike[6]	Dip[7]	ΔStrike[8]	ΔDip[9]	ΔStrike[10]	ΔDip[11]
Fag1	240	47–61			*	114 (105/125), 15	−87 (−58/57), 15	7 (0/17), 6	31 (19/44), 6		31 (9/58), 5
Fag2	234	7.5–7.5		*-Fo	*	131 (120/142), 8	−77 (−65/ − 88), 8	1 (0–2), 2	12 (11/13), 2		8 (0/13), 4
Fau1	47	7.5–7.5	*			111 (105/112), 5	76 (−82/43), 5	<	24 (0/42), 3		
Fau2	102	3.5–7.5		*		79 (74/84), 3	85 (−75/68), 8		18 (0/28), 3		13 (6/19), 2
Fs1	287	18.5–22		*	*	166	86 (−78/70), 9		3 (0/14), 6		10 (2/32), 6
Fs2	214	17–25.5	*-Fo	*	*	164	−89 (−80/78), 8		1(0/6), 6		7 (0/22), 5
Fs5	296	37–50	*-Fo		*	176 (161/18), 4	90 (−59/64), 9		27(9/67), 4		10 (0/20), 2
Fs3	27	1.5–9	*-Fo		*	108 (80/135), 2	88 (87/89), 2				
Fs6	119	15–24			*	150 (131/174), 5	74 (−84/62), 5		<		20 (13/33), 3
Fv1	196	27–28			*	3 (162/22), 11	81 (−86/54), 11	15 (9–21), 2	21 (2/40), 2	9 (1/15), 3	5 (1/9), 3
Fv2	290	23–26.5			*	143 (135/150), 9	74 (−72/22), 9	7 (3–12), 3	21 (15/26), 3	6 (2/10), 2	47 (28/66), 2
Fv3	88	13.5–13.5		*		20 (15/25), 2	74 (−88,57), 2				

[1]Vertical length of the fault.
[2]Maximal near-field and far-field observed displacements.
[3, 4]Lower and upper tips observed with fold ahead (Fo) or not.
[5]Fold achieving part of far-field displacement. Note that * in [3, 4, 5] denotes positive items.
[6, 7]Fault strike and dip.
[8, 9]Variations within one bed of the fault strike and the fault dip.
[10, 11]Variations through a bed interface of the fault strike and the fault dip. In [6–11], the first number and the two numbers in brackets are the mean, and the minimum and maximum values. The last number indicates the number of data.
< denotes negligible variations.

and Jurassic and Early Cretaceous gravity deposits (e.g. slumps, debris flows) that indicate permanent slope instabilities associated with recurrent tectonic activity (Dardeau *et al.* 1988; Joseph *et al.* 1989; Friès & Parize 2003; Courjault *et al.* 2011; Homberg *et al.* 2013). Normal faulting of the Kimmeridgian–Valanginian sequences exposed in the study area is not reflected in striations on the fault surfaces, a feature we attribute to the weakly lithified state of the sediments at the time of faulting.

Notably, most of the studied faults show a sinuous shape, as observed in cross-section, with large variations in their dips. These variations are up to 55°, 65°, 67° and 86° along Fau1, Fag1, Fs5 and Fv2, respectively (Fig. 7; Table 1). Fault refraction as a function of the lithology, referred to here as the 'bed-to-bed' sinuosity, contributes to this irregular fault shape. The largest dip variations are observed within individual beds ('in-bed' fault sinuosity), so that the fault dip progressively increases or decreases, sometimes even changing its dip direction across a bed. Note that, except in the Villeperdrix sections, each limestone bed is generally homogeneous. In addition, 'in-bed' fault sinuosity varies along a given fault, so that straight, sinuous and very sinuous segments occur even on faults that cut a rather homogeneous sequence. This is particularly obvious on Fag1, Fau1, Fau2, Fs5 and Fv1, for which the 'in-bed' sinuosity (variations within individual beds) range equals 19°–44°, 0°–42°, 0°–28°, 9°–67°, 2°–40°, respectively (Fig. 7a; Table 1). Thus, there seems to be no correlation between the very pronounced fault sinuosity and the mechanical layering as observed today.

Near-field displacement profiles

Displacement data measured in the direct vicinity of the faults were used to construct near-field displacement profiles. Although the faults are generally only partly exposed, characteristic displacement patterns are recognized (Fig. 8). An abrupt decrease in displacement is observed at the lower tips of Fs5 and Fau1, the upper tips of Fs1 and Fag2, and both tips of Fs2 and Fau2 (but with another segment ahead of the tip). An overall upwards and downwards decrease from a maximal value (D_{max} point) is observed on Fs2, Fs5, Fv1, Fv2, Fag2 and Fau2, which is likely to indicate that the central parts of these faults have been mapped. Although the profiles may be irregular in detail, their overall shapes exhibit either a triangular or a flat-topped profile, defined according to the following nomenclature. Triangular profiles are composed of two straight lines along which the displacement decreases from the D_{max} point to zero at the two fault tips, the displacement gradient is thus constant along each half of the fault. Flat-topped profiles have a long, low-displacement gradient, central plateau and much higher gradients near the fault tips. The first type characterizes isolated faults in homogeneous media, whereas flat-topped profiles denote complexities in fault growth, such as restriction by lithological interface or interaction with neighbouring faults (Peacock 1991; Wilkins & Gross 2002; Roche *et al.* 2012*b*).

Fs2, Fs5 and Fv2 show half near-field triangular profiles along their exposed lengths, and isolated tips with gradients equal to 0.1, 0.34 and 0.22,

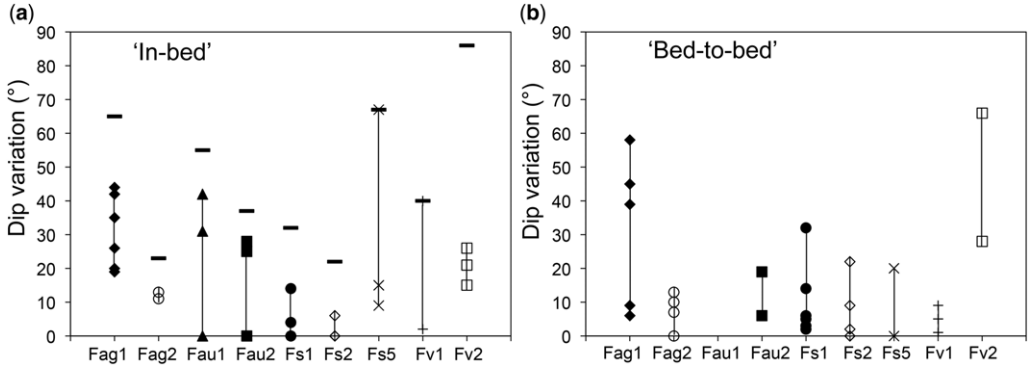

Fig. 7. Fault dip variability v. mechanical layering. (**a**) 'In-bed' dip variations. Each symbol indicates the maximum change of fault dip within one homogeneous limestone bed. The short and thick horizontal bar denotes the maximum variation observed on the exposed part of the fault. (**b**) 'Bed-to-bed' dip variations. Each symbol indicates the change in the fault dip from one side to another of a bed interface. In most cases, the 'bed-to-bed' variations are moderate, whereas the 'in-bed' variations are high, indicating that changes in the fault dip barely correlate with the mechanical stratigraphy but occur within a homogeneous bed. Fag1 and Fag2, faults in Agnielles; Fau1 and Fau2, faults in Aulan; Fs1, Fs2, Fs3, Fs5 and Fs6, faults in Sahune; Fv1, fault in Villeperdrix1; Fv2 and Fv3, faults in Villeperdrix2. See also Table 1. See Figure 3 for the site location.

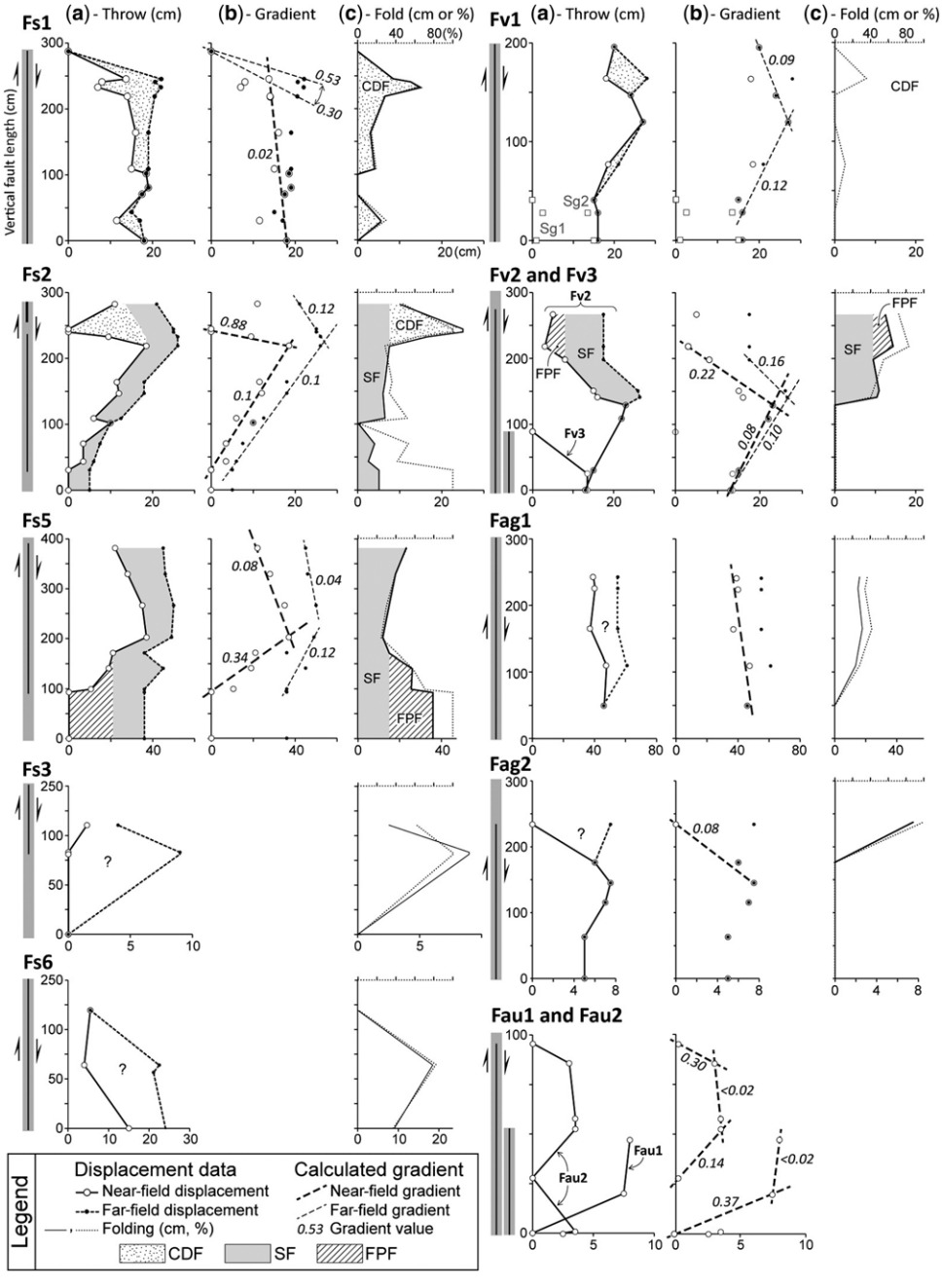

Fig. 8. Displacement data. (**a**) Displacement profiles. (**b**) Gradient data. (**c**) Contribution of folding to the total displacement. Near-field and far-field displacements represent the displacement achieved, respectively, by faulting and by both faulting and folding (see Fig. 2 for the measurement of displacement data). Dashed lines in (b) show how local near-field and far-field gradient values discussed in the text are calculated. The left thin black line and thick grey band denote the vertical extent of the fault and of the folded zone. The folding component is generally above 20% and greater than 40% along several fault portions. Shading indicates the amount of folding associated with coherent drag folding (CDF), shear folding (SF) or fault-propagation folding (FPF). A dominant mechanism explains most of the folding component of a given fault, but a second mechanism may be superposed locally. See also Table 2.

respectively (Fig. 8). Although the profiles of Fs5 and Fv2 are incomplete, these faults are clearly asymmetrical. Available data along the partly exposed halves of these faults yield a gradient of 0.08 for both. If these gradients are used to extrapolate the displacement profile to the supposed isolated fault tip, a local gradient up to four times greater than that on the exposed half will be noticed, indicating an asymmetry in the profile. Fs2 is characterized by an even more pronounced asymmetry, with gradients equal to 0.88 and 0.1 along the upper and lower fault tips, attributed to interaction with the other fault segment on the upper part of the section. Fs1, Fag2 and Fau1 show flat-topped profiles along their upper, upper and lower tips, respectively, with near-tip gradients equal to 0.3 (or more), 0.08 and 0.37. Fau2 shows a complete flat-topped profile with near-tip gradients equal to 0.14 (lower tip) and 0.30 (upper tip). The local gradient near the central part of the fault is estimated to be below 0.02 on Fs1, Fau1 and Fau2. All these gradient values are subject to uncertainties related to the limited exposure of most faults, as well as the distance separating displacement markers. Despite this limitation, the values obtained here show some consistency. In fine-grained homogenous carbonates (the Sahune, Aulan and Agnielles sections: see 'Mesoscale normal faults in the Southeast Basin of France' earlier in this paper), the near-tip gradient data define two peaks, at 0.08–0.14 and at 0.3–0.4. The lower peak is close to values calculated by others along isolated faults in similar lithologies (Soliva *et al.* 2005; Roche *et al.* 2012*b*). In the Villeperdrix sections, where coarse beds are also present, they range between 0.08 and 0.22, without an apparent preferred value.

Far-field displacement profiles and fault-related folding

Fault-related folds were observed along all the studied faults (e.g. see Fig. 5), except for Fau1, Fau2 and Fv3. The displacement data discussed combine near-field data (i.e. the discontinuous offset: Fig. 8a), far-field data (i.e. the sum of the displacement achieved by faulting and folding: Fig. 8a), as well as the folding contribution to the total bed offset, referred to as the folding component (Fig. 8c). The folding component is variable along each fault, generally above 20% and greater than 40% along half or more of the exposed lengths of Fs1, Fs2, Fs5, Fs3, Fs6 and Fv2. A large part of the displacement along the investigated fault zones is thus achieved by folding, although the host rocks consist mostly of fine-grained limestones beds which may be expected to be stiff. Below the lower tip of Fs2, Fs5 and Fs3, and above the upper tip of Fs2 and Fag2, the folding component reaches 100%.

The closely spaced measurements along Fs1, Fs2, Fs5, Fv2, Fag1 and Fag2 allow comparison between the far-field and near-field displacement distribution. The overall shape of the far-field displacement profiles along these faults is similar to that of the near-field profiles. Along Fs1 and Fs2, small-scale fluctuations of the near-field displacement are superposed on the overall flat-topped and triangular shapes of the profiles, whereas the far-field profiles are much less variable. Generally, variations in the displacements achieved by folding and faulting are complementary and balance each other partly or fully. This is highlighted on the displacement profiles by the coincidence of local maxima in the near-field displacement with minima in the folding component curves (cf. Fig. 8a, b), whereas the far-field curves are almost straight. The amplitude of these fluctuations is generally moderate, but can occasionally be very high similar to that observed along the upper part of Fs2. In this case, the near-field displacement is locally zero and the vertical displacement of the beds there is achieved exclusively by folding. These relationships between the brittle and ductile components of the deformation highlight that both of these components are linked and together constitute a coherent fault zone. Fs1 and Fs2 thus exhibit coherent drag folds, as described in the earlier section 'Conceptual models of near-field and far-field displacements along blind normal faults' (Fig. 2c).

In addition to the small-scale fluctuations described above, other patterns of the displacement and folding component curves are observed. Below the lower tip of Fs5 and the upper tip of Fv2 (2 cm of brittle displacement still observed), the folding component curves show a plateau ahead of these fault tips, a configuration that is consistent with a fault-propagation fold (Fig. 2a). The folded zone extends vertically along a length that represents at least 25% of the fault height. A similar mechanism may explain the fold observed ahead of the upper tip of Fag2, but there the fold amplitude increases slightly away from the tip.

The near-field and far-field displacement data show similar relationships below the lower tip of Fs2, so that a fault-propagation folding may explain, on first inspection, the fold observed ahead of the fault tip. Examination of the complete displacement profile, however, suggests an alternative interpretation. Along the lower half of Fs2, the far-field values are always greater than the near-field ones. Folding is thus observed over a significant fault height and at the likely place of fault nucleation marked today by the D_{max} point of the near-field profile. In addition, the near-field and far-field profiles show almost identical gradients of 0.1. The two curves indicate that the folding component is almost constant along the length of the fault zone. This configuration

is consistent with the development of a shear zone later cut by a brittle fault (Fig. 2b, c). Fs5 and the upper portion of Fv2 may also be explained by this model. In these cases, the fault throw and the total displacement (near-field and far-field data: Fig. 8a, b) both decrease from a maximum value with the same D_{max} point but with different slopes. Along the two upper halves of Fv2 and Fs5, and the lower half of the Fs5, the far-field gradients are 0.16, 0.04 and 0.12, respectively, and are smaller than the near-field gradients, with values of 0.22, 0.08 and 0.34. Near these fault tips, the displacement profile is characterized by an increasing component of folding that may represent a variation in the shear model.

Discussion

Summary of fault characteristics

The mesoscale normal faults observed in the Southeast Basin of France show the following characteristics:

- Fault-related folds were observed at different levels along the fault zones, from their central part to their tips (Figs 5 & 8). The amplitude of the folding component (normal drag) is variable along the fault plane, but mostly accounts for a significant part of the total throw. Folds extend a few decimetres to a few metres into the fault walls and along a distance of more than 25% of the fault height ahead of the fault tip.
- Fault-related folds affect stiff and compliant (rare) layers, and no relationship between the folding amplitude and the rock lithology is apparent.
- The fault planes are sinuous, even though the faults are cutting through a homogeneous medium that consists of a succession of fine-grained limestone beds (mostly mudstones–wackestones). When coarser-grained limestones are interbedded with marly intervals, fault refractions across bed interfaces may occur, but the largest fault dip variations are due to pronounced fault sinuosity (progressive variation) within individual beds (Table 1).
- The near-field (brittle component) and far-field (sum of brittle and ductile components) displacement profiles follow either flat-topped or triangular shapes independent of lithology (Fig. 8). The displacement gradients near the fault tips are generally high and commonly above 0.3 (Table 2).
- The fault planes rarely exhibit striations.

Diagnostic values of displacement profiles

A comparison of displacement profiles reconstructed on mesoscale normal faults allows the identification of three different types of fault-related folding: (1) fault-propagation folds; (2) coherent drag folds; and (3) shear folds (Table 2). Among the criteria that distinguish between these fold mechanisms, abrupt variations in the near-field displacement with an otherwise regular far-field displacement distribution characterize coherent drag folds (Figs $5c_2$ & 8). In the case of fault-propagation folding, divergence of the near-field and far-field curves at a point distant from the D_{max} point of the near-field profile (left-hand plots in Fig. 8) marks the tip of a folded zone with an almost constant amplitude (no high-frequency variation). A long vertical folded zone also characterizes faults with ductile shear that preceded the discontinuous offset (shear folds). In this case, the far-field displacements always exceed the near-field (Fig. 8). The coherent drag-fold model supports previous work which demonstrated that some faults and their associated volumes of deformation have been kinematically coherent throughout their evolution (Walsh *et al.* 2003; Long & Imber 2010). This points to the necessity of integrating the off-fault deformation in the analysis of fault growth and thus examine their far-field displacement profiles. Possibly, some folds in the published literature that are attributed to drag developed according to the 'coherent fault' model described here.

The analysis of mesoscale normal faults presented here demonstrates that it is possible to recognize several folding mechanisms that are superposed along the same fault (Table 2). However, the distinctive signature of each folding mechanism described, and potentially others, may be difficult to distinguish in a number of geological situations: for instance, for faults that developed in heterogeneous rocks, spatial and temporal variations in fault strength and local stresses. 2D sections close to the lateral tips of faults also represent complex cases. Hence, it is critical to define to what extent the proposed models can be applied to natural faults to allow prediction of the distribution and amplitude of fault-related folds: such as for the analyses of sub-seismic faults, for example. Further quantitative studies investigating the folding component along fault zones are therefore needed to improve our understanding of fault-related folding.

Folding and hosting rock

Fault-related folding is commonly better developed in compliant rocks. Accordingly, the folding component observed along the investigated faults is the largest in sequence Fs5, comprising the thickest clay-rich layers (Fig. 4a). In this case, the folding extends along the full fault height. However, except for Fs5, no apparent relationship between the fault-related folds and the rock lithology and

Table 2. *Fold mechanisms and gradient data*

	Fold type	Near-field displacement data					Far-field displacement data				
		Type	$Grdt_L$	$Grdc_L$	$Grdt_U$	$Grdc_U$	Type	$Grdt_L$	$Grdc_L$	$Grdt_U$	$Grdc_U$
Fag1	?	∼Flat					∼Flat				
Fag2	FPF?	Unk/FTo			0.08		∼Flat				
Fau1	/	FTo/Unk	0.37	<0.02			FTo/Unk	0,37	<0.02		
Fau2	/	FTo/FTo	0.14	<0.02	0.30	<0.02	FTo/FTo	0,14	<0.02	0,30	<0.02
Fs1	CDF	Unk/FTo			0.30	0.02	Unk/FTo			0,30–0,53	flat
Fs2	CDF + SF	Tr/Tr	0.1	–	0.88	–	Be/Unk		0.1–0		0.12
Fs5	SF + FPF	Tr/Tr?	0.34	–	–	0.08	Be?/Unk		0.12–0		0.04
Fv1	CDF?	Be/Unk		0.12–0		0.09	Be/Unk		0.12–0		0.09
Fv2	SF + FPF	Unk/Be		0.08		0.22–0	Unk/Be		0.1		0.16–0

Fold mechanism identified along the fault zones are fault-propagation fold (FPF), shear fold (SF) and coherent drag fold (CDF).
'Type' in the displacement data denotes the overall shape of the displacement profiles (lower/upper part of the fault): Tr, FTo, Bell and Unk: triangular, flat-topped, bell and unknown shapes.
Grdt and Grdc are gradient values close to the fault tips and along the central part of the fault, respectively. Superscript letters U and L refer to the upper and lower part of the fault.
Values followed by '− 0'indicate that the displacement decrease is followed by a plateau. This profile shape is informally named a bell profile (Be).

thickness of the beds was observed. Therefore, we propose that the rocks were only partially lithified at the time of faulting. The mechanical layering was thus different to that observed today. This hypothesis is further discussed in the following sub-section. In indurated rocks, clay-rich layers are among the most common lithology favouring folding. The pattern of the stacking of competent and incompetent units is also likely to play an important role. As a function of these parameters, we expect shear folds to be developed in a dominantly compliant pile, coherent drag folds in alternating stiff and compliant units, and fault-propagation folds in both dominantly stiff rocks covered by a compliant unit and in alternating stiff and compliant units.

Published near-field displacement gradients measured along isolated faults in stiff and fine-grained limestones, with no fault-related folds are around 0.08 (Soliva *et al.* 2005; Roche *et al.* 2012*a*). Those obtained in this study (Table 2) are much higher, generally above 0.22 (Fv1 and Fag2 excluded). These values are in agreement with those of Ferrill & Morris (2008), who concluded that in heterogeneous carbonate sequences the less competent units impede fault propagation, promoting high near-field displacement gradients and fault-related folding. Considering all the gradient values cited above, a minimum 0.2 gradient value may be proposed for the development of fault-related folds in carbonate-rich sediments.

Other fault characteristics and relationship with rock properties

Even though the depth of faulting is not constrained, faulting in some of the studied sections (e.g. Fv2, Fv3, Fs1, Fs2 and Fs5) is likely to have occurred shortly after the sediments were deposited. These north–south faults developed in the Kimmeridgian–Tithonian formations before the Late Tithonian–Berriasian major tectonic reorganization in the Southeast Basin of France, after which the extension adopted a NNE–SSW direction (Homberg *et al.* 2013). Owing to the large (up to 75%) folding component observed along these faults, we suggest that they formed before the complete lithification of the sediments, which were more compliant than today. This is in line with the up to 0.3 near-field displacement gradients measured along the triangular displacement profiles of Fs5 and Fv2, a value to be compared to the 0.012–0.25 gradient found along faults formed in poorly lithified sandstones (Wibberley *et al.* 1999). A similar pronounced sinuosity as the one observed along the studied faults (Fig. 4; Table 1) has also been described for faults formed before the complete lithification of massive sandstones and medium- to high-energy shallow platform carbonates (Petit & Laville 1987; Koša & Hunt 2005; Bergerat *et al.* 2011). We suggest that high-frequency variations in the fault dip, observed together with a large folding component and the absence of penetrative striae, may be used to recognize faults that grew before complete lithification of carbonates.

Conclusions

Analysis of mesoscale normal faults combined with conceptual models of fault growth allowed the contribution of fault-related folding to the total fault displacement to be quantified. The mechanism that caused folding may change along the fault height. Three different mechanisms were identified by comparing variations in the folding and fault-slip components along the fault height: fault-propagation folds; shear folds; and coherent drag folds. Abrupt variations in the near-field (i.e. fault-slip) displacement with an otherwise regular far-field (sum of brittle and ductile components) displacement profile indicate complementary variations between fault slip and folding; large folding components in specific fault portions can be used to distinguish between these types of fold. The folding component along the investigated faults is generally greater than 20% and up to 75% of the total displacement. Compliant units and high near-field displacement gradients along the faults have promoted folding, and the stacking pattern of the competent and incompetent units is likely to have played a major role in the occurrence of a specific folding process.

We are grateful to David Ferrill, an anonymous reviewer and Conrad Childs for their suggestions that helped us to greatly improve the manuscript. We thank Ramadan Ghalayini, who enhanced the quality of the English text and Alexandre Lethiers for drawing the figures.

References

Allmendinger, R.W. 1998. Inverse and forward numerical modeling of trishear fault propagation folds. *Tectonics*, **17**, 640–656.

Allmendinger, R.W. & Shaw, J.H. 2000. Estimation of fault propagation distance from fold shape: implications for earthquake hazard assessment. *Geology*, **28**, 1099–1102.

Angelier, J. 1990. Inversion of field data in fault tectonics to obtain the regional stress – III. A new rapid direct inversion method by analytical means. *Geophysical Journal International*, **103**, 363–376.

Benzaggagh, M. & Atrops, F. 1995*a*. Les zones à *Chitinoidella* et à *Crassicollaria* (Tithonien) dans la partie interne du Prérif (Maroc). Données nouvelles et corrélation avec les zones d'ammonites. *Comptes Rendus de l'Academie des Sciences, Paris*, **320**, 227–234.

Benzaggagh, M. & Atrops, F. 1995*b*. Données nouvelles sur la succession des calpionelles du Berriasien

dans le Prérif et le Mésorif (Rif, Maroc). *Comptes Rendus de l'Academie des Sciences, Paris*, **321**, 631–638.

Bergerat, F. 1987. Stress fields in the European platform at the time of Africa–Eurasia collision. *Tectonics*, **6**, 99–132.

Bergerat, F., Collin, P.-Y., Ganzhorn, A.-C., Baudin, F., Galbrun, B., Rouget, I. & Schnyder, J. 2011. Instability structures, synsedimentary faults and turbidites, witnesses of a Liassic seismotectonic activity in the Dauphiné Zone (French Alps): a case example in the Lower Pliensbachian at Saint-Michel-en-Beaumont. *Journal of Geodynamics*, **51**, 344–357.

Brandes, C. & Tanner, D.C. 2014. Fault-related folding: a review of kinematic models and their application. *Earth-Science Reviews*, **138**, 352–370.

Calamita, F., Pace, P. & Satolli, S. 2012. Coexistence of fault-propagation and fault-bend folding in curve-shaped foreland fold-and-thrust belts: examples from the Northern Apennines (Italy). *Terra Nova*, **24**, 396–406.

Carreras, J., Druguet, E. & Griera, A. 2005. Shear zone-related folds. *Journal of Structural Geology*, **27**, 1229–1251.

Cloos, H. 1936. *Einführung in die Geologie*. Gebrüder Bornträger, Berlin.

Courjault, T., Grosheny, D., Ferry, S. & Sausse, J. 2011. Detailed anatomy of a deep-water carbonate breccia lobe (Upper Jurassic, French subalpine basin). *Sedimentary Geology*, **238**, 156–171.

Dardeau, G., Atrops, F., Fortwengler, D., de Graciansky, P.-C. & Marchand, D. 1988. Jeu de blocs et tectonique distensive au Callovien et à l'Oxfordien dans le bassin du Sud-Est de la France. *Bulletin de la Societe Géologique de France*, **8**, 771–777.

Debrand-Passard, S., Courbouleix, S. & Lienhardt, M.-J. 1984. *Synthèse géologique du Sud-Est de la France*. Mémoires du Bureau de Recherches geologiques et minieres, **125–126**.

Dubois, P. & Delfaud, J. 1989. Le Bassin du Sud-Est. *In*: *Dynamique et méthodes d'étude des bassins sédimentaires. Association des Sédimentologistes français*. Technip, Paris, 277–296.

Erslev, E.A. 1991. Trishear fault-propagation folding. *Geology*, **19**, 617–620.

Ferrill, D.A. & Morris, A.P. 2003. Dilational normal faults. *Journal of Structural Geology*, **25**, 183–196.

Ferrill, D.A. & Morris, A.P. 2008. Fault zone deformation controlled by carbonate mechanical stratigraphy, Balcones fault system, Texas. *American Association of Petroleum Geologists Bulletin*, **92**, 359–380.

Ferrill, D.A., Morris, A.P., Sims, D.W., Waiting, D.J., Hasegawa, S. 2005. Development of synthetic layer dip adjacent to normal faults. *In*: Sorkhabi, R. & Tsuji, Y. (eds) *Faults, Fluid Flow, and Petroleum Traps*. American Association of Petroleum Geologists, Memoirs, **85**, 125–138.

Ferrill, D.A., Morris, A.P. & Smart, K.J. 2007. Stratigraphic control on extensional fault propagation folding: big Brushy Canyon monocline, Sierra Del Carmen, Texas. *In*: Jolley, S., Barr, D., Walsh, J. & Knipe, R. (eds) *Structurally Complex Reservoirs*. Geological Society, London, Special Publications, **292**, 203–217, https://doi.org/10.1144/SP292.12

Ferrill, D.A., Morris, A.P., McGinnis, R.N., Smart, K.J. & Ward, W.C. 2011. Fault zone deformation and displacement partitioning in mechanically layered carbonates: the Hidden Valley fault, central Texas. *American Association of Petroleum Geologists Bulletin*, **95**, 1383–1397.

Ferrill, D.A., Morris, A.P. & McGinnis, R.N. 2012. Extensional fault-propagation folding in mechanically layered rocks: the case against the frictional drag mechanism. *Tectonophysics*, **576–577**, 78–85.

Finch, E., Hardy, S. & Gawthorpe, R. 2004. Discrete-element modelling of extensional fault propagation folding above rigid basement fault blocks. *Basin Research*, **16**, 489–506.

Flandrin, J. 1975. *Carte géologique de la France à 1:50 000. 891, Nyons, Sheet XXXI-39*. Bureau de Recherches geologiques et minieres, Orléans, France.

Friès, G. & Parize, O. 2003. Anatomy of an ancient passive margin slope system: Aptian gravity-driven deposition on the Vocontian paleomargin, western Alps, south-east France. *Sedimentology*, **50**, 1231–1270.

Ghalayini, R., Homberg, C., Daniel, J.M. & Nader, F.H. 2016. Growth of layer-bound normal faults under a regional anisotropic stress field. *In*: Childs, C., Holdsworth, R.E., Jackson, C.A.-L., Manzocchi, T., Walsh, J.J. & Yielding, G. (eds) *The Geometry and Growth of Normal Faults*. Geological Society, London, Special Publications, **439**, first published online April 6, 2016, https://doi.org/10.1144/SP439.13

Gawthorpe, R.L., Sharp, I., Underhill, J.R. & Gupta, S. 1997. Linked sequence stratigraphic and structural evolution of propagating normal faults. *Geology*, **25**, 795–798.

Graciansky, P.-C. de & Lemoine, N. 1988. Early Cretaceous extensional tectonics in the southwestern French Alps: a consequence of North-Atlantic rifting during Tethyan spreading. *Bulletin de la Societe Géologique de France*, **IV**, 733–737.

Grasemann, B., Martelb, S. & Passchier, C. 2005. Reverse and normal drag along a fault. *Journal of Structural Geology*, **27**, 999–1010.

Homberg, C., Schnyder, J. & Benzaggagh, M. 2013. Late Jurassic–Early Cretaceous faulting in the Southeastern French Basin: does it reflect a tectonic reorganization? *Bulletin de la Société Géologique de France*, **184**, 501–514.

Janecke, S.U., Vandenburg, C.J. & Blankenau, J.J. 1998. Geometry, mechanisms and significance of extensional folds from examples in the Rocky Mountain Basin and Range province, USA. *Journal of Structural Geology*, **20**, 841–856.

Joseph, P., Beaudoin, B., Friès, G. & Parize, O. 1989. Les vallées sous-marines enregistrent au Crétacé inférieur le fonctionnement en blocs basculés du domaine vocontien. *Comptes Rendus de l'Academie des Sciences, Paris*, **309**, 1031–1038.

Koledoye, B.A., Aydin, A. & May, E. 2003. A new process-based methodology for analysis of shale smear along normal faults in the Niger Delta. *American Association of Petroleum Geologists Bulletin*, **87**, 445–463.

Koša, E. & Hunt, D.W. 2005. Growth of syndepositional faults in carbonate strata: Upper Permian Capitan platform, New Mexico, USA. *Journal of Structural Geology*, **27**, 1069–1094.

Lemoine, M., de Graciansky, P.-C. & Tricart, P. 2000. *De l'océan à la chaîne de montagnes. Tectonique des plaques dans les Alpes*. SGF Collection Géosciences. Gordon & Breach, Paris.

Long, J.J. & Imber, J. 2010. Geometrically coherent continuous deformation in the volume surrounding a seismically imaged normal fault-array. *Journal of Structural Geology*, **32**, 222–234.

Mandl, G. 1988. *Mechanics of Tectonic Faulting: Model and Basic Concept*. Elsevier, New York.

Mansfield, C.S. & Cartwright, J.A. 1999. Stratal fold patterns adjacent to normal faults: observations from the Gulf of Mexico. *In*: Cosgrove, J.W. & Ameen, M.S. (eds) *Forced Folds and Fractures*. Geological Society, London, Special Publications, **169**, 115–128, https://doi.org/10.1144/GSL.SP.2000.169.01.09

McClay, K.R. 1992. *Thrust Tectonics*. Chapman & Hall, London.

Muraoka, H. & Kamata, H. 1983. Displacement distribution along minor fault traces. *Journal of Structural Geology*, **5**, 483–485.

Nicol, A., Gillespie, P.A., Childs, C. & Wash, J. 2002. Relay zones between mesoscopic thrust faults in layered sedimentary sequence. *Journal of Structural Geology*, **24**, 709–727.

Peacock, D. 1991. Displacement and segment linkage in strike–slip fault zones. *Journal of Structural Geology*, **13**, 1025–1035.

Peacock, D.C.P. & Parfitt, E.A. 2002. Active relay ramps and normal fault propagation on Kilauea Volcano, Hawaii. *Journal of Structural Geology*, **24**, 29–742.

Petit, J.-P. & Laville, E. 1987. Morphology and microstructures of hydroplastic slickensides in sandstone. *In*: Jones, M.E. & Preston, R.M.F. (eds) *Deformation of Sediments and Sedimentary Rocks*. Geological Society, London, Special Publications, **29**, 107–121, https://doi.org/10.1144/GSL.SP.1987.029.01.10

Remane, J. 1971. Les Calpionelles, Protozoaires planctoniques des mers mésogéennes de l'époque secondaire. *Annales Guébhard, Neuchâtel*, **47**, 1–25.

Roche, V., Homberg, C. & Rocher, M. 2012*a*. Architecture and growth of normal fault zones in multilayer systems: a 3D field analysis in the South-Eastern Basin, France. *Journal of Structural Geology*, **37**, 19–35.

Roche, V., Homberg, C. & Rocher, M. 2012*b*. Fault displacement profiles in multilayer systems: from fault restriction to fault propagation. *Terra Nova*, **24**, 499–504, https://doi.org/10.1111/j.1365-3121.2012.01088.x

Rotevatn, A. & Jackson, C.A.-L. 2014. 3D structure and evolution of folds during normal fault dip linkage. *Journal of the Geological Society, London*, **171**, 821–829, https://doi.org/10.1144/jgs2014-045

Rouire, J., Gidon, M. *et al.* 1980. *Carte géologique de la France au 1/250 000, feuille 34: Valence*. Bureau de Recherches geologiques et minieres, Orléans, France.

Schlische, R.W. 1995. Geometry and Origin of Fault-Related Folds in Extensional Settings. *American Association of Petroleum Geologists Bulletin*, **79**, 1661–1678.

Schöpfer, M.P.J., Childs, C., Walsh, J.J., Manzocchi, T. & Koyi, H.A. 2007. Geometrical analysis of the refraction and segmentation of normal faults in periodically layered sequences. *Journal of Structural Geology*, **29**, 318–335.

Smart, K.J., Ferrill, D.A., Morris, A.P. & McGinnis, R.N. 2012. Geomechanical modelling of stress and strain evolution during contractional fault-related folding. *Tectonophysics*, **576**, 171–196.

Soliva, R., Schultz, R.A. & Benedicto, A. 2005. Three-dimensional displacement–length scaling and maximum dimension of normal faults in layered rocks. *Geophysical Research Letters*, **32**, L16302, https://doi.org/10.1029/2005GL023007

Suppe, J. 1983. Geometry and kinematics of fault-bend folding. *American Journal of Science*, **283**, 684–721.

Suppe, J. & Medwedeff, D.A. 1990. Geometry and kinematics of fault-propagation folding. *Eclogae Geologicae Helvetiae*, **83**, 409–454.

Walsh, J.J. & Watterson, J. 1987. Distributions of cumulative displacement and seismic slip on a single normal fault surface. *Journal of Structural Geology*, **9**, 1039–1046.

Walsh, J.J., Bailey, W.R., Childs, C., Nicol, A. & Bonson, C.G. 2003. Formation of segmented normal faults: a 3D perspective. *Journal of Structural Geology*, **25**, 1251–1262.

Wibberley, A.J., Petit, J.-P. & Rives, T. 1999. Mechanics of high displacement gradient faulting prior to lithification. *Journal of Structural Geology*, **21**, 251–257.

Wilkins, S.J. & Gross, M.R. 2002. Normal fault growth in layered rocks at Split Mountain, Utah: influence of mechanical stratigraphy on dip linkage, fault restriction and fault scaling. *Journal of Structural Geology*, **24**, 1413–1429.

Withjack, M.O., Olson, J. & Peterson, E. 1990. Experimental models of extensional forced folds. *American Association of Petroleum Geologists Bulletin*, **74**, 1038–1054.

Zoetemeijer, R., Sassi, W., Roure, F. & Cloetingh, S. 1992. Stratigraphic and kinematic modeling of thrust evolution, northern Apennines, Italy. *Geology*, **20**, 1035–1038.